J Physiol 591.19 (2013) pp 4843–4858

JPn Neuroscience

The Journal of Physiology

Ba^{2+}- and bupivacaine-sensitive background K^+ conductances mediate rapid EPSP attenuation in oligodendrocyte precursor cells

Chu-Fang Chan[1], Tzu-Wei Kuo[1], Ju-Yun Weng[1], Yen-Chu Lin[1,3], Ting-Yu Chen[1], Jen-Kun Cheng[3] and Cheng-Chang Lien[1,2]

[1] *Institute of Neuroscience and* [2] *Brain Research Center, National Yang-Ming University, Taipei 11221, Taiwan*
[3] *Department of Medicine, Mackay Medical College, New Taipei City 25245, Taiwan*

Key points

- We developed detailed passive cable models of rat oligodendrocyte precursor cells (OPCs) based on dual somatic recordings and complete morphological reconstructions.
- Both specific membrane capacitance and specific axial resistivity are comparable to those of central neurons, but the average specific membrane resistance (R_m ~4.1 kΩ cm^2) is substantially lower in OPCs.
- Large Ba^{2+}- and bupivacaine-sensitive background K^+ conductances contribute to the low R_m.
- Simultaneous dual soma and process whole-cell recordings reveal powerful voltage attenuation along OPC processes, indicating that OPC processes are a strong voltage attenuator.
- The low R_m also sharpens EPSPs and thus narrows the temporal window for EPSP integration.

Abstract Glutamatergic transmission onto oligodendrocyte precursor cells (OPCs) may regulate OPC proliferation, migration and differentiation. Dendritic integration of excitatory postsynaptic potentials (EPSPs) is critical for neuronal functions, and mechanisms regulating dendritic propagation and summation of EPSPs are well understood. However, little is known about EPSP attenuation and integration in OPCs. We developed realistic OPC models for synaptic integration, based on passive membrane responses of OPCs obtained by simultaneous dual whole-cell patch-pipette recordings. Compared with neurons, OPCs have a very low value of membrane resistivity, which is largely mediated by Ba^{2+}- and bupivacaine-sensitive background K^+ conductances. The very low membrane resistivity not only leads to rapid EPSP attenuation along OPC processes but also sharpens EPSPs and narrows the temporal window for EPSP summation. Thus, background K^+ conductances regulate synaptic responses and integration in OPCs, thereby affecting activity-dependent neuronal control of OPC development and function.

(Received 16 April 2013; accepted after revision 5 August 2013; first published online 12 August 2013)
Corresponding author C.-C. Lien: Institute of Neuroscience, National Yang-Ming University, 155, Section 2, Li-Nong Street, Taipei 11221, Taiwan. Email: cclien@ym.edu.tw

Abbreviations AMPAR, AMPA receptor; C_m, specific membrane capacitance; DGC, dentate granule cell; $GABA_AR$, $GABA_A$ receptor; GFAP, glial fibrillary acidic protein; IR-DIC, infrared and differential interference contrast; Kir channel, inwardly rectifying K^+ channel; mEPSP/EPSC, miniature EPSP/EPSC; NG2, nerve/glial antigen-2; NMDAR, *N*-methyl-D-aspartate receptor; OL, oligodendrocyte; OPC, oligodendrocyte precursor cell; R_i, specific axial resistance; R_m, specific membrane resistance; R_N, input resistance; R_s, series resistance; τ_m, membrane decay time constant; TASK channel, TWIK-related acid-sensitive K^+ channel; Z_c, transfer impedance; Z_N, input impedance.

C.-F. Chan, T.-W. Kuo, J.-Y. Weng, Y.-C. Lin and T.-Y. Chen contributed equally to this work.

DOI: 10.1113/jphysiol.2013.257113

Introduction

Oligodendrocyte precursor cells (OPCs) are the fourth major type of glia besides astrocytes, oligodendrocytes (OLs) and microglia (Nishiyama *et al*. 2009). Although most types of glial cells respond in some way to extracellular neurotransmitter molecules, only OPCs receive classical synaptic input from neurons (Bergles *et al*. 2000; Ge *et al*. 2006; De Biase *et al*. 2010). Neurons make excitatory glutamatergic synapses with OPCs and generate rapid excitatory postsynaptic potentials (EPSPs) exclusively onto their processes (Bergles *et al*. 2000; Haberlandt *et al*. 2011). Glutamate receptor activation has been shown to alter the proliferation, migration and differentiation of OPCs *in vitro* (Gallo *et al*. 1996; Yuan *et al*. 1998; Gudz *et al*. 2006). However, the electrical function of these EPSPs, a major depolarizing signalling in OPCs, is not yet known.

OPCs have a unique stellate morphology, with fine and highly branched dendrite-like processes that radially extend from a small cell body (Bergles *et al*. 2000; Gallo *et al*. 2008). The frequent close apposition of OPC processes to axo-spinous synapses revealed by electron microscopy raises the possibility that these cells receive neuronal signalling from their processes and modulate neuronal synaptic transmission (Bergles *et al*. 2000; Haberlandt *et al*. 2011). Furthermore, OPCs are highly dynamic; they survey their local environment with motile filopodia, extend growth cones and continuously migrate (Hughes *et al*. 2013). The small diameter of the processes and filopodia renders them electrically isolated from the expanse of the soma. The actual dynamics of EPSPs in OPC processes and terminal branches, however, are entirely unclear because electrode recording from such small structures is not feasible. EPSPs generated in remote processes are relatively large and may contribute to local Ca^{2+} signalling in the processes through enhancement of *N*-methyl-D-aspartate receptor (NMDAR) and voltage-gated Ca^{2+} (Ca_v) channel activity (Haberlandt *et al*. 2011) and thus influence their dynamic behaviour and function. In order to modulate OPC function, rapid EPSPs arising from different synaptic sites must be integrated. However, in contrast to central neurons, the factors mediating EPSP attenuation along OPC processes and their integration are completely unknown.

To address these questions, a clear view of the passive electrotonic 'skeleton' of these cells, the foundation upon which EPSP attenuation and integration takes place, is required. In this study, we anatomically reconstructed five OPCs and converted them into detailed compartmental models. Passive electrical cable parameters including specific membrane resistance (R_m), specific axial resistance (R_i) and specific membrane capacitance (C_m) were optimized by direct fitting of the model responses to the electrophysiological data from the same cell. Compared with mammalian central neurons, OPCs had a markedly low value of R_m, which was largely contributed by Ba^{2+}- and bupivacaine-sensitive K^+ channels. Analysis of OPC cable models revealed that large background K^+ conductances not only mediate powerful voltage attenuation along OPC processes, but also narrow the integration window for EPSP summation.

Methods

Ethical approval

All surgical and experimental procedures were performed in accordance with ethical standards as outlined in Drummond (2009) as well as with the National Institutes of Health *Guide for the Care and Use of Laboratory Animals*. The experimental protocol was reviewed and approved by the Institutional Animal Care and Use Committee of National Yang-Ming University.

Electrophysiology

Male Sprague–Dawley rats (19–28 postnatal days) were killed by rapid decapitation by appropriately trained researchers. In brief, their brains were rapidly removed and 300 μm thick transverse hippocampal slices were cut in ice-cold cutting saline solution (in mM: 87 NaCl, 25 $NaHCO_3$, 1.25 NaH_2PO_4, 2.5 KCl, 10 glucose, 75 sucrose, 0.5 $CaCl_2$ and 7 $MgCl_2$) using a vibratome (DTK-1000, Dosaka, Kyoto, Japan). Slices were incubated in the oxygenated (95% O_2 and 5% CO_2) cutting saline in a holding chamber at 34°C for 40 min and finally stored at room temperature until used. During experiments, slices were placed in a recording chamber and superfused with oxygenated artificial cerebral spinal fluid (ACSF) containing (in mM): 125 NaCl, 25 $NaHCO_3$, 1.25 NaH_2PO_4, 2.5 KCl, 25 glucose, 2 $CaCl_2$ and 1 $MgCl_2$. Recording electrodes (3–12 MΩ) were pulled from borosilicate glass (outer diameter, 1.5 mm; wall thickness, 0.32 mm; Harvard Apparatus, Edenbridge, UK). Putative OPCs were first identified in the CA1 stratum radiatum by their small round somata (diameter < 10 μm) under an infrared and differential interference contrast (IR-DIC) microscope (Axioskop 2 FS, Zeiss, Oberkochen, Germany or BX51WI, Olympus, Tokyo, Japan) and then by their electrophysiological characteristics. Whole-cell recordings were made using an Axopatch 200B or a Multiclamp 700B amplifier (Molecular Devices, Sunnyvale, CA, USA). Dual whole-cell patch-clamp recordings were made using a Multiclamp 700B amplifier. Pipette capacitances of both electrodes were carefully compensated (by >95%) and series resistance (R_s) was compensated using the automatic bridge balance (readouts after compensation were

5–16 MΩ). Signals were filtered at 4 or 10 kHz except where noted using the 4-pole low-pass Bessel filter. A Digidata 1332A or 1440A connected to a personal computer was used for stimulus generation and data acquisition. The sampling frequency was 10–50 kHz. Pulse sequences were generated by pCLAMP 9 or 10.2 (Molecular Devices). No correction for liquid junction potentials was made. All recordings were made at 22–24°C.

Immunohistochemistry

Staining of biocytin-filled OPCs with Alexa 594-conjugated streptavidin (1:400; Invitrogen, Carlsbad, CA, USA) was performed as described previously (Lin *et al.* 2010). Nerve/glial antigen-2 (NG2)-immunostaining was done with a mouse-anti-NG2 primary antibody (1:200; Abcam, Cambridge, UK) and a goat-anti-mouse-Alexa 488 secondary antibody (1:500; Invitrogen). Slices were fixed after recording in 4% paraformaldehyde in 0.01 M phosphate-buffered saline (PBS) overnight. After washing in PBS, slices were permeabilized with 0.3% Triton X-100 and then blocked in PBS + 10% normal goat serum (NGS, 2 h at 4°C). The primary antibody was applied in PBS + 0.3% Triton X-100 + 5% NGS (48 h at 4°C), and the secondary antibody was incubated together with streptavidin conjugate in PBS + 0.3% Triton X-100 + 2% NGS for 2 h at 4°C. After washing, slides were coverslipped with mounting medium Vectashield (Vector Laboratories, Burlingame, CA, USA). For double immunofluorescence, primary antibodies against NG2 (mouse, 1:200; Abcam), Olig2 (rabbit, 1:500; Millipore, Billerica, MA, USA), glial fibrillary acidic protein (GFAP; rabbit, 1:400; Dako, Glostrup, Denmark), Iba-1 (rabbit, 1:500; Wako Chemicals, Osaka, Japan) and secondary antibodies (goat anti-rabbit-Alexa 488, 1:500 for Olig2, GFAP and Iba-1; goat anti-mouse-Alexa 350, 1:200) for NG2 were used. Slices were imaged by two-photon microscopy as described previously (Lin *et al.* 2010).

Solutions and drugs

The intracellular solution for whole-cell recordings contained (in mM): 120 potassium gluconate, 20 KCl, 10 EGTA, 2 $MgCl_2$, 2 Na_2ATP, 10 Hepes and 0.2% biocytin; pH adjusted to 7.3 with KOH (Nörenberg *et al.* 2010). In whole-cell recording experiments except miniature EPSP/EPSC (mEPSP/mEPSC) and compound EPSP recordings, kynurenic acid (2 mM), gabazine (1 μM) and tetrodotoxin (TTX, 0.5 μM) were included to block α-amino-3-hydroxy-5-methyl-4-isoxazolepropionic acid receptors (AMPARs) and NMDARs, $GABA_A$-receptor ($GABA_AR$)-mediated neurotransmission and voltage-gated sodium (Na_V) channels, respectively. All other chemicals were purchased from Sigma-Aldrich (St Louis, MO, USA) except where noted.

Direct measurement of R_m and C_m

A direct approach for measuring R_m and C_m was applied as previously described (Gentet *et al.* 2000). Briefly, nucleated patches isolated from OPCs were lifted close to the surface of the bath to reduce the pipette capacitance (Fig. 5*A* and *B*). A −5 mV pulse (5 ms) was applied from a membrane potential of −80 mV and more than 2000 capacitance transients were recorded and averaged (Fig. 5*C*, trace (1)). To record fast transients, signals were made to bypass the low-pass filter and sampled at 200 kHz using a Multiclamp 700B amplifier. At the end of the recording, the patch was blown away and the open tip of the pipette was pressed against a small Sylgard ball, resulting in a giga-ohm seal. The depth of the pipette in the bath solution was not changed. Again, a −5 mV pulse was applied and the transient, which was due to charging of the residual uncompensated pipette capacitance, was averaged (Fig. 5*C*, trace (2)). The residual capacitance transient was subtracted from the capacitive transient recorded from the nucleated patch. The amplitude, decay time constant and steady-state level of this transient (Fig. 5*C*, trace (1 – 2)) can be analysed to estimate the R_s of the recording pipette, the patch membrane resistance (R_p), and patch membrane capacitance (C_p; Fig. 5*A*).

$$R_s = V_{step}/I_{peak}$$

$$R_p = V_{step}/I_{ss} - R_s$$

$$C_p = \tau_{decay}(1/R_s + 1/R_p)$$

where V_{step} is the amplitude of the voltage (V)-clamp step, I_{peak} is the peak amplitude of the current transient immediately after the step is applied, τ_{decay} is the decay time constant of the current, and I_{ss} is the steady-state current at longer times following the step. These parameters τ_{decay}, I_{peak} and I_{ss} were determined by fitting a single exponential function with an added constant to the current transient recorded during the voltage step. To obtain R_m, the value of R_p was multiplied by the surface area of the patch. By contrast, the value of C_p was divided by the measured surface area to calculate C_m (Gentet *et al.* 2000).

Measurement of miniature events and compound EPSPs

Hypertonic solution (500 mM sucrose in ACSF) was focally applied by a glass pipette to force vesicular release of glutamate from nerve terminals in the presence of antagonists for Na_v channels (TTX, 0.5 μM) and $GABA_ARs$ (gabazine, 1 μM; De Biase *et al.* 2010). The hypertonic solution containing puffer pipette (1–2.5 MΩ; pulled from

borosilicate glass) was placed 10–20 μm from the soma of the recorded cell. The puff (10 s duration; 10–20 kPa) was applied by a PicoSpritzer III (Parker Instrumentation, Pine Brook, NJ, USA) triggered by an external TTL pulse generated by the Digidata 1332A. Compound EPSPs were evoked by a 0.1 ms pulse delivered by a stimulus isolator (Isoflex, A.M.P.I., Jerusalem, Israel) at 0.033 Hz with a glass electrode positioned in the CA1 stratum radiatum in the presence of antagonists for $GABA_A$Rs (gabazine, 1 μM), $GABA_B$Rs (CGP 55845, 1 μM) and NMDARs (D-aminophosphonovalerate (D-AP5), 20 μM). To study temporal summation of EPSPs, two compound EPSPs were evoked using a pair of pulses separated by intervals from 10 to 50 ms. Signals were filtered at 2–4 kHz, and then digitized at 10 kHz.

Image acquisition and 3-D reconstruction of OPCs

For 3-D reconstruction of biocytin-labelled cells, high-resolution two-photon images of OPCs were acquired. Labelled OPCs were examined by a two-photon microscope using a pulsed titanium:sapphire laser (Chameleon-Ultra II tuned to 800 nm; Coherent, Santa Clara, CA, USA) attached to a Leica DM6000 CFS (Leica, Wetzlar, Germany) that was equipped with a ×63/0.9 NA water immersion objective (objective type HCX APO L). The morphology of the cells was reconstructed from a stack of 91–188 images per cell (voxel size, 60–72 nm in the x–y plane; 0.3–0.5 μm along the z-axis). Image stacks belonging to one cell were imported into the Neuromantic 1.6.3 software (Myatt *et al.* 2012) for 3-D reconstruction. Analysis of morphological parameters was performed using Neurolucida Explorer (MicroBrightField, Williston, VT, USA).

Detailed cable modelling and simulations

Passive electrical cable models were obtained using NEURON 7.2 (Hines & Carnevale, 1997) running under Windows 7.0 on a PC. The digitized morphological data were exported in NEURON format. Segment length was adjusted according to the 'd_lambda rule' (Carnevale & Hines, 2006) as follows. The alternating current (AC) length constant at 1 kHz (λ_{1kHz}) was calculated for each section, and the number of segments per section (n_{seg}) was increased until the length of segments was below 10% of λ_{1kHz}. Further increasing n_{seg} by a factor of 3 had no effect on the results of the simulations. The integration time step was fixed to 125 μs. Frequency-dependent voltage attenuation was computed using NEURON's built-in impedance tools (Hines & Carnevale, 1997). R_m, C_m and R_i were obtained by direct least-squares fitting of the response of the model to the experimental data in NEURON using the built-in 'Brent's principal axis' algorithm that minimizes the sum of squared errors ('error values' in NEURON). To constrain cable model parameters, voltage responses to brief and long current pulses were used. The initial phase (2 ms from the onset of response) of the brief response representing the fast charge redistribution was weighted by a factor of ∼4.7 to ensure a match of the brief voltage response and to increase the contribution of R_i to the goodness of the total fit (Nörenberg *et al.* 2010). For passive cable models based on dual somatic recordings, only traces from the voltage-recording electrode were used. Although thick-walled pipette glass and capacitance compensation were used, a residual capacitive component of the pipette tips might contribute to the recorded voltage signals (Roth & Häusser, 2001). Therefore, residual pipette capacitance was included as an additional free parameter into the fits, and their total axial resistance was adjusted so that it matched the R_s (Nörenberg *et al.* 2010). The average of best-fit values for the total capacitance of our pipette models was 0.20 ± 0.09 pF ($n = 5$), indicating that the capacitance of the pipette electrodes was well compensated during the experiments. Synaptic AMPA receptor conductance changes with the maximal conductance of 1 nS were simulated using the sum of two exponential functions with τ_{rise} of 0.25 ms and τ_{decay} of 1 ms and a reversal potential of 0 mV (Bergles *et al.* 2000). When a V-clamp was simulated at the soma of an OPC model, synaptic AMPA receptor conductance changes with these kinetics led to somatic V-clamp currents that decayed with time constants between 1.2 ms (proximal synapses) and 1.7 ms (distal synapses), which is in close agreement with measured EPSCs ($\tau_{decay} = 1.56 \pm 0.13$ ms, $n = 5$ cells; see Fig. 9*B*) in OPCs obtained under whole-cell V-clamp conditions.

Data analysis and statistics

Data were analysed using Clampfit 10.2 (Molecular Devices) and Prism 5.0 (GraphPad Software, San Diego, CA, USA). Miniature events were analysed using Mini Analysis Program software (Synaptosoft, Leonia, NJ, USA); each event was inspected and events containing significant noise artifacts were rejected. Traces in the figures were single or averages of 26–108 sweeps except the traces of average miniature responses (as indicated in the text) and passive voltage response, which were averages of >250 sweeps. Data are presented as mean ± standard error of mean (SEM). Error bars equal SEM and were plotted only when they exceeded the respective symbol size. Statistical significance was tested by the Wilcoxon signed-rank or Wilcoxon rank-sum test at the significance level (P) as indicated, using Prism 5.0.

Results

Identification of NG2$^+$ OPCs

OPCs, also known as NG2 cells, express the cell type-specific surface marker nerve/glial antigen-2 (NG2) proteoglycan (Bergles *et al*. 2000). Therefore, we recorded putative OPCs in the stratum radiatum of CA1 area filled with biocytin, and performed immunofluorescence labelling against the NG2 protein. In this study, only cells which were identified *post hoc* by their immunoreactivity to NG2 were included. NG2$^+$ OPCs located in the stratum radiatum of area CA1 exhibited a relatively negative resting potential (V_{rest}) of -85.7 ± 1.3 mV ($n = 68$), a modest input resistance (R_N) of 136.5 ± 12.7 MΩ ($n = 72$), large A-type and delayed rectifier K^+ currents, and did not fire action potentials (Fig. 1*A*). The large majority (78%; $n = 55$) of OPCs displayed a small membrane bump at stronger depolarization (Fig. 1*A*). Consistent with previous reports, OPCs with all-or-none spikes were not observed in this area (Ge *et al*. 2006; Lin *et al*. 2010).

Post hoc morphological analysis revealed that recorded cells had the morphological characteristics of NG2-expressing glial cells (Fig. 1*B*). They had a small polygonal soma with multiple highly branched processes. The mean process length was $37.9 \pm 2.6\ \mu$m ($n = 5$ cells) and the maximal length was up to ~99 μm from the soma (see Table 1). In addition to NG2 staining, some recorded cells were immunolabelled with antibodies against Olig2 (a marker for OPC lineage), Iba-1 (a marker for microglia) and GFAP (a marker for astrocytes). Analysis of immunofluorescence revealed that all of the cells (3/3 cells) were immunopositive for Olig2, but were immunonegative for Iba-1 (0/7 cells) or GFAP (0/4 cells; Fig. 1*C*).

Passive membrane properties of OPCs

To examine the passive membrane properties, we measured the voltage responses by applying current pulses (Fig. 2*A*, top) to the recorded cells at the V_{rest} in the presence of antagonists for Na_v channels (TTX, 0.5 μM), AMPARs (kynurenic acid, 2 mM) and $GABA_A$Rs (gabazine,1 μM). Positive voltage responses ($V_{m,pos}$) were the mirror images of negative voltage responses ($V_{m,neg}$) evoked by both short and long pulse protocols. Consistently, the normalized positive ($V_{m,pos}/I_{inj}$) and negative ($V_{m,neg}/I_{inj}$) responses were almost identical (Fig. 2*A*, bottom). Voltage responses to short pulse current injection reflect the major charge of the somatic membrane area. By contrast, long pulse current injection induces voltage responses through charging the entire cell surface. Analysis of the voltage decay induced by either a short or a long current pulse yielded a similar membrane decay time constant (τ_m) (26 cells; Fig. 2*B*), strongly suggesting uniform R_m distribution over the entire OPC surface (Schmidt-Hieber *et al*. 2007; Nörenberg *et al*. 2010). Furthermore, the electrotonic architecture of OPCs can be considered a single compartment model.

If R_m is non-uniform and current is injected into the low R_m region, local voltage transients will decay more rapidly than remote transients (Nörenberg *et al*. 2010). Thus, to further confirm uniform R_m in OPCs, we compared the decay time course of process and somatic voltage transients evoked by brief current injection. Simultaneous recordings from the soma and the process during brief somatic current injections revealed that the somatic and process traces converged during the decay phase of the transient (Fig. 2*C*, left). We also injected brief current pulses into the process and recorded process and somatic voltage responses (Fig. 2*C*, right). Although the voltage transient in the process was substantially larger, the late

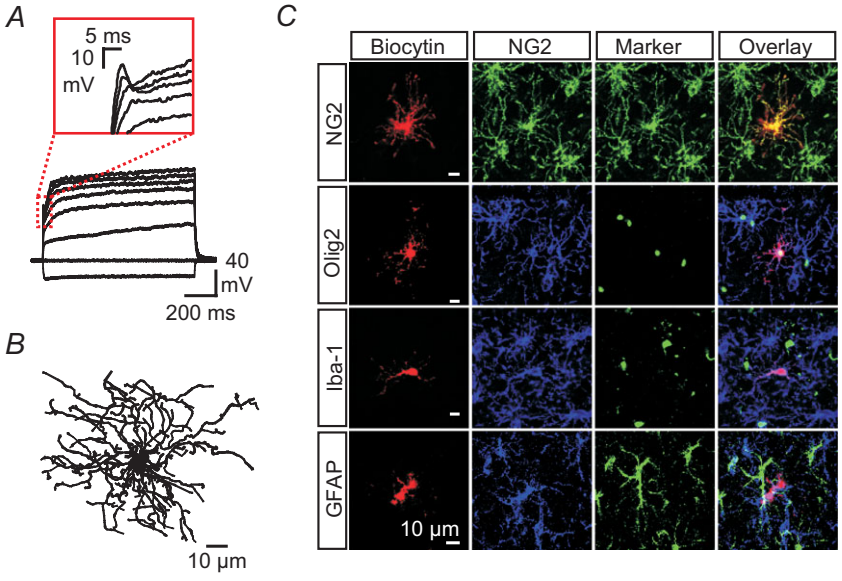

Figure 1. Cell identification and characteristics of NG2$^+$ OPCs
A, voltage responses to 1 s current pulses (−100 pA to +600 pA; step, 100 pA) in the whole-cell current clamp recording configuration. Membrane potential before the pulse was −80 mV. *B*, reconstruction of a biocytin-filled OPC, the same cell as described in *A*. *C*, immunofluorescence labelling of biocytin$^+$ OPCs, which were immunopositive to NG2 and Olig2, but immunonegative to Iba-1 and GFAP.

Table 1. Morphological properties of reconstructed OPCs

Parameter	OPC-1	OPC-2	OPC-3	OPC-4	OPC-5	Mean ± SEM
Total surface area (μm^2)	4124.1	3427.9	2852.8	3423.4	3379.6	3441.6 ± 202.1
Total cell volume (μm^3)	1092.8	747.4	754.4	675.2	499.7	753.9 ± 96.4
Soma						
Soma major axis (μm)	10.7	10.8	9.8	8.8	10.3	10.1 ± 0.4
Soma minor axis (μm)	9.1	8.3	9.1	5.5	5.0	7.4 ± 0.9
Soma surface area (μm^2)	277.8	226.1	247.7	129.1	117.7	199.7 ± 32.3
Soma volume (μm^3)	417.6	280.8	343.5	136.5	100.6	255.8 ± 60.3
Process						
Total length (μm)	1956.8	2454.0	1641.9	1854.3	2434.3	2068.3 ± 161.7
Total area (μm^2)	3846.3	3201.8	2605.1	3294.3	3262.0	3241.9 ± 196.9
Total volume (μm^3)	675.2	466.6	410.9	538.7	399.1	498.1 ± 50.7
Mean process length (μm)	37.0	47.6	36.6	35.5	32.6	37.9 ± 2.6
Maximum process length (μm)	70.2	99.2	77	69.4	56.2	74.4 ± 7.1
No. of segments	237	347	226	283	350	288.6 ± 26.3
Average segment length (μm)	8.3	7.1	7.3	6.6	7.0	7.2 ± 0.3
Average width of process tree (μm)	0.61	0.42	0.51	0.57	0.44	0.51 ± 0.04
Average initial diameter (μm)	1.58	0.91	1.41	1.03	0.82	1.15 ± 0.15
No. of branch points	108	165	108	130	164	135.0 ± 12.7
Maximum branch order	10	18	12	15	12	13.4 ± 1.4
Number of process terminals	129	182	118	153	186	153.6 ± 13.7
Number of trees	17	11	7	19	12	13.2 ± 2.2

Morphologies were reconstructed by Neuromantic and analysed using Neurolucida Explorer.

phase of somatic and process transients rapidly converged. Together, these results are consistent with dual recordings of granule cells, suggesting a homogeneous distribution of membrane properties (Schmidt-Hieber *et al.* 2007).

Development of OPC cable models by dual-pipette patch-clamp recordings

The voltage changes from the V_{rest} of OPCs in response to small hyper- or depolarizing currents display a linear relationship in the presence of synaptic blockers (Fig. 2*A* and *B*). To evoke voltage changes from the V_{rest} without a R_s compensation artifact, we made dual-pipette patch-clamp recordings from the soma (Fig. 3*A*) and the biocytin-filled cells were reconstructed after recordings. The voltage transient with electrode artifact was recorded from the current-feeding electrode (blue trace; Fig. 3*B* and *C*), whereas the voltage response was recorded from the voltage-recording electrode (black trace; Fig. 3*B* and *C*) and was used for cable fitting. During recording, the

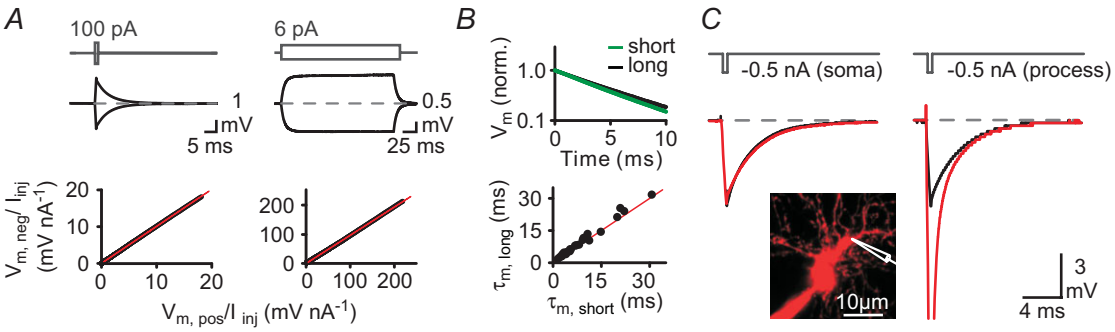

Figure 2. Passive membrane properties of OPCs
A, top, voltage responses evoked by short (±100 pA, 0.5 ms) and long pulses (±6 pA, 200 ms). Bottom, amplitude of hyperpolarizing responses was plotted against that of depolarizing responses at the same time point. Note that data points were close to the identity line (red). *B*, top, semi-logarithmic plot of the normalized decay responses evoked by short and long pulses. Bottom, plot of membrane time constant (τ_m) measured from short and long pulses. *C*, left, a brief (0.5 ms) somatic current injection evoked voltage responses at the soma (black) and at a process (red) 14 μm from the centre of the soma. Note similar somatic and dendritic voltage decays. Right, voltage response at the process (red) and at the soma (black) when a brief current pulse was applied to the process. The inset shows the location of the somatic and the process pipettes.

pipette capacitance and access resistance of both electrodes were automatically compensated in bridge-balanced mode. To reliably estimate the cytoplasmic resistivity, i.e. the value of R_i, we injected brief depolarizing pulses (0.5 ms; Fig. 3*B*). The initial fast transient reflects the initial charge redistribution (Nörenberg *et al.* 2010), whereas the τ_{decay} of the slow transient represents the membrane time constant ($\tau_m = R_m C_m$). To constrain the R_m, we evoked the steady-state voltage responses by injecting 500 ms current pulses (Fig. 3*C*) because steady-state voltage changes were solely determined by R_m and the injecting current amplitude. Thus, to obtain the R_i, R_m and C_m, we simultaneously fitted both short (Fig. 3*D*) and long transients (Fig. 3*E*) with the anatomically detailed compartmental models which were converted from five reconstructed cells (Table 2; see the details in Methods). Because analysis of decay responses induced by short and long current pulses yielded a very similar τ_m (Fig. 2*B*), cable parameters were thus considered to be homogeneously distributed over the OPC surface (Schmidt-Hieber *et al.* 2007; Nörenberg *et al.* 2010). Simultaneous fits of both short and long voltage transients to the multiple compartmental models based on the morphology of the recorded cells (Fig. 3*F* for the fits of cells 2, 3 and 4; only short-pulse fits were shown; also see Fig. 4*I* for the fits of cell 5) yielded the best-fit parameters. The mean values were: R_m, $4.1 \pm 1.1\ k\Omega\ cm^2$ (range, 1.9–7.5 $k\Omega\ cm^2$); C_m, $1.2 \pm 0.1\ \mu F\ cm^{-2}$ (1.1–1.4 $\mu F\ cm^{-2}$); and R_i, $146.6 \pm 21.5\ \Omega$ cm (93.1–215.1 Ω cm) ($n = 5$; Table 2). The fitted responses (Fig. 3*D*–*F*; red traces) superimposed well with the experimental data, confirming that the OPCs are well described by passive compartmental models with uniform parameters (Roth & Häusser, 2001; Schmidt-Hieber *et al.* 2007; Nörenberg *et al.* 2010).

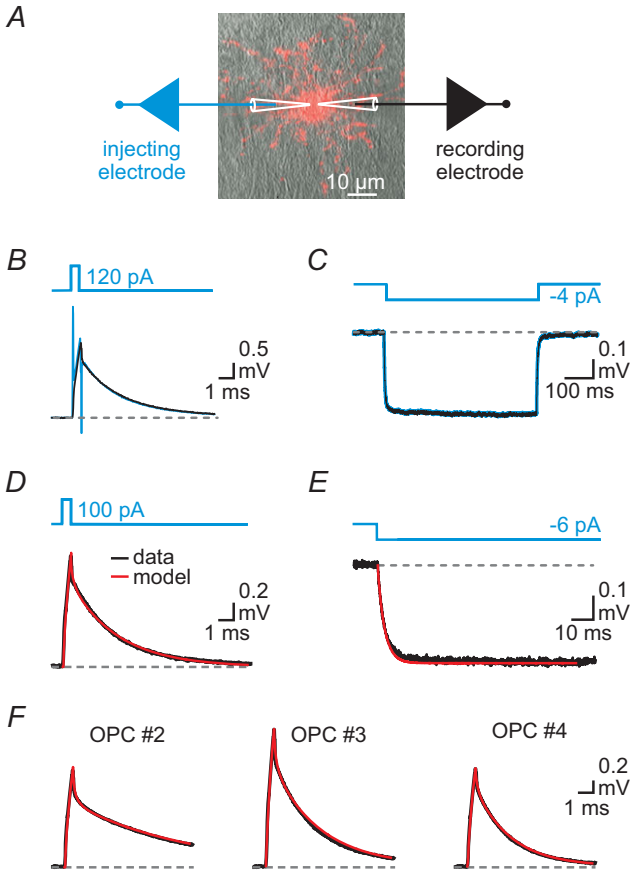

Figure 3. Matching OPC models to experimental data obtained by dual somatic recording
A, overlay of an IR-DIC image of two patch pipettes attached to an OPC soma with the fluorescence image of the same cell (biocytin-filled) stained with Alexa 594-conjugated streptavidin. *B*, voltage responses to a brief (0.5 ms) current pulse; blue trace recorded from current-feeding pipette; black trace recorded from voltage-recording pipette. *C*, similar to *B*, voltage responses to a long (500 ms) current pulse. *D*, voltage response to a brief (0.5 ms) current pulse. Raw data (black) superimposed with the fit of the model (red). *E*, voltage response to a long pulse and the fit of the model. *F*, raw data and best-fits of three other OPCs.

Ionic basis of low membrane resistivity

OPCs have a relatively negative V_{rest} (about −86 mV) and a low value of R_m, strongly suggesting that large background K^+ conductances including inwardly rectifying K^+ (Kir) and tandem-pore TWIK-related acid-sensitive K^+ (TASK)-like channels may contribute to the leaky membrane property (Taverna *et al.* 2005; Chu *et al.* 2010). Consistent with this notion, it has been reported that OPCs express Kir channels (Chittajallu *et al.* 2004; Maldonado *et al.* 2013). Although no specific inhibitors of Kir or TASK-like channels exist, the conductance of recombinant Kir or TASK-like channels is decreased by extracellular Ba^{2+} and bupivacaine (Zhou *et al.* 2001; Taverna *et al.* 2005; Chu *et al.* 2010). To directly probe the ionic basis underlying the low value of R_m, we applied Ba^{2+} or bupivacaine and then measured the change of R_N. In whole-cell recordings (Fig. 4*A*), extracellular Ba^{2+} resulted in a dose-dependent increase of R_N (a 15-fold increase by 100 μM Ba^{2+}; Fig. 4*B*, from $125 \pm 33\ M\Omega$ to $1890 \pm 397\ M\Omega$, $n = 13$; $P < 0.001$, Wilcoxon signed-rank test), concomitant with an increase in τ_m (Fig. 4*C*, from 5.6 ± 1.3 to 79.5 ± 10.9 ms, $n = 13$; $P < 0.001$, Wilcoxon signed-rank test). In line with the notion of K^+ channel blockade, the Ba^{2+}-sensitive current component in whole-cell recordings exhibited a reversal potential of −81.3 mV (Fig. 4*D*). Similar to Ba^{2+}, bupivacaine had significant effects on R_N (Fig. 4*E* and *F*, from 117.6 ± 27.3 to 2529 ± 586.7 MΩ, $n = 7$; $P < 0.05$, Wilcoxon signed-rank test) and τ_m (Fig. 4*E* and *G*, from 5.7 ± 1.0 to 80.1 ± 12.8 ms, $n = 7$; $P < 0.05$, Wilcoxon signed-rank test). Furthermore, the current–voltage (I–V) relationship of bupivacaine-sensitive current was similar

Table 2. Best-fit cable parameters of OPCs

Parameter	OPC-1	OPC-2	OPC-3	OPC-4	OPC-5[b]	Mean ± SEM
Age (days)	24	27	22	24	19	23.2 ± 1.3
Recording configuration[a]	D-S	D-S	D-S	D-S	D-S	–
R_N (MΩ)	68.1	177.7	97.1	58.8	218.3	124.0 ± 31.5
τ_m (ms) (short/long pulse)	2.7/2.9	7.3/8.2	2.7/3.4	2.1/2.5	8.7/9.8	4.7 ± 1.4/5.4 ± 1.5
No. of traces averaged	289	266	297	288	56	239.2 ± 46.0
R_m (kΩ cm^2)	2.8	5.7	2.5	1.9	7.5	4.1 ± 1.1
C_m (μF cm^{-2})	1.1	1.3	1.2	1.2	1.4	1.2 ± 0.1
R_i (Ω cm)	167.5	93.1	142.3	111.6	215.1	146.0 ± 21.5

[a]D-S, dual somatic recording. [b]After addition of 100 μM Ba^{2+}, the best-fit values for R_m, C_m and R_i were 77.8 kΩ cm^2, 1.2 μF cm^{-2} and 222 Ω cm, respectively.

to Ba^{2+}-sensitive current (Fig. 4*H*; reversal potential −82.3 mV). Taken together, our results indicate that the resting membrane conductances of OPCs are largely mediated by Ba^{2+}- and bupivacaine-sensitive background K^+ channels.

Finally, we sought to test whether Ba^{2+} could also lead to a large increase of R_m as determined by the cable-fitting approach. As seen in Fig. 4*I*, bath application of Ba^{2+} (100 μM) remarkably prolonged the decay responses evoked by both short and long current pulses. Indeed, simultaneous fits of both short and long responses resulted in a 10-fold increase of R_m (from 7.5 to 77.8 kΩ cm^2), with little change of C_m and R_i (see Table 2).

As an alternative to the cable-fitting approach, we directly determined passive membrane properties (i.e. R_m and C_m) from the nucleated patches as previously described (Gentet *et al.* 2000). The mean values of R_m and C_m were 5.19 ± 0.81 kΩ cm^2 (range, 1.85–9.84 kΩ cm^2; $n = 10$) and 1.04 ± 0.09 μF cm^{-2} (range, 0.75–1.57 μF cm^{-2}; $n = 10$), respectively (Fig. 5*A*–*E*). To test the validity of this method, we measured the R_m of dentate granule cells (DGCs) using the same approach. The mean values of R_m (49.8 ± 20 kΩ cm^2, $n = 4$) and C_m (1.02 ± 0.13 μF cm^{-2}, $n = 4$) were very similar to those obtained from the fits of voltage transients to cable models (Schmidt-Hieber *et al.* 2007; Wilcoxon rank-sum test, both P values > 0.3; data not shown). In nucleated patch recordings, bath application of Ba^{2+} to OPC nucleated patches resulted in a ∼16-fold increase in R_m (control, 5.19 ± 0.81 kΩ cm^2, $n = 10$ *vs.* 100 μM Ba^{2+}, 86.46 ± 10.69 kΩ cm^2, $n = 8$; $P < 0.0001$, Wilcoxon rank-sum test; Fig. 5*F*) without significant changes in C_m (control, 1.04 ± 0.09 μF cm^{-2}, $n = 10$ *vs.* 100 μM Ba^{2+}, 1.05 ± 0.05 μF cm^{-2}, $n = 8$; $P = 0.9$, Wilcoxon rank-sum test; Fig. 5*F*). Notably, the Ba^{2+}-sensitive current component evoked by the ramp voltage protocols exhibited a reversal potential of −86.0 mV in nucleated patch recordings (Fig. 5*G*), close to the reversal potential for K^+ currents. Overall, the direct measurement of R_m indicates that OPCs have a very leaky membrane property at rest, in agreement with the best-fit values of cable models (Table 2).

Electrotonic analysis of OPC cable models

Our results indicate that the values of R_m of OPCs obtained under the same or similar conditions to previous studies (Schmidt-Hieber *et al.* 2007; Nörenberg *et al.* 2010) are strikingly low (see Discussion), despite the modest input resistance of OPCs. To investigate signal processing in these thin and highly branched processes, we first performed a detailed electrotonic analysis of OPC models. Synaptic AMPA receptor conductance changes (G_{max} of 1 nS) were simulated using the sum of two exponential functions with τ_{rise} of 0.25 ms and τ_{decay} of 1 ms and a reversal potential of 0 mV (Bergles *et al.* 2000). Simulated synapses were placed along the processes and the resulting local EPSPs were plotted against the distance to soma (Fig. 6*A*). The local EPSP amplitude increased rapidly with the distance to soma, consistent with the spatial profile of local input impedance (Z_N; Fig. 6*B*). As predicted from the cable theory (Rall, 1964), although the EPSP (red) generated at the distal synapse was large, its amplitude was strongly attenuated along the process (Fig. 6*C*). The time course of an EPSP also became slow as it approached the soma (Fig. 6*C*).

The voltage transfer ratio $k_{syn\rightarrow soma}$ represents the degree of voltage attenuation from synapse to soma, i.e. $V_{process}/V_{syn}$, where V_{syn} is the local EPSP amplitude at the synaptic location and $V_{process}$ is the amplitude along the process (Carnevale & Johnston, 1982). Here, $k_{syn\rightarrow soma}$ declined rapidly from synapse to soma, yielding a small EPSP amplitude (about 20-fold attenuation) at the soma (Fig. 6*D*). However, if a synapse was placed along the process (Fig. 6*E*), its ability to alter somatic membrane potential (V_{soma}) was much less dependent on the synapse location (Fig. 6*F*; blue line represents the path shown in Fig. 6*E*). Such a phenomenon is called 'passive normalization of EPSPs' (Jaffe & Carnevale, 1999).

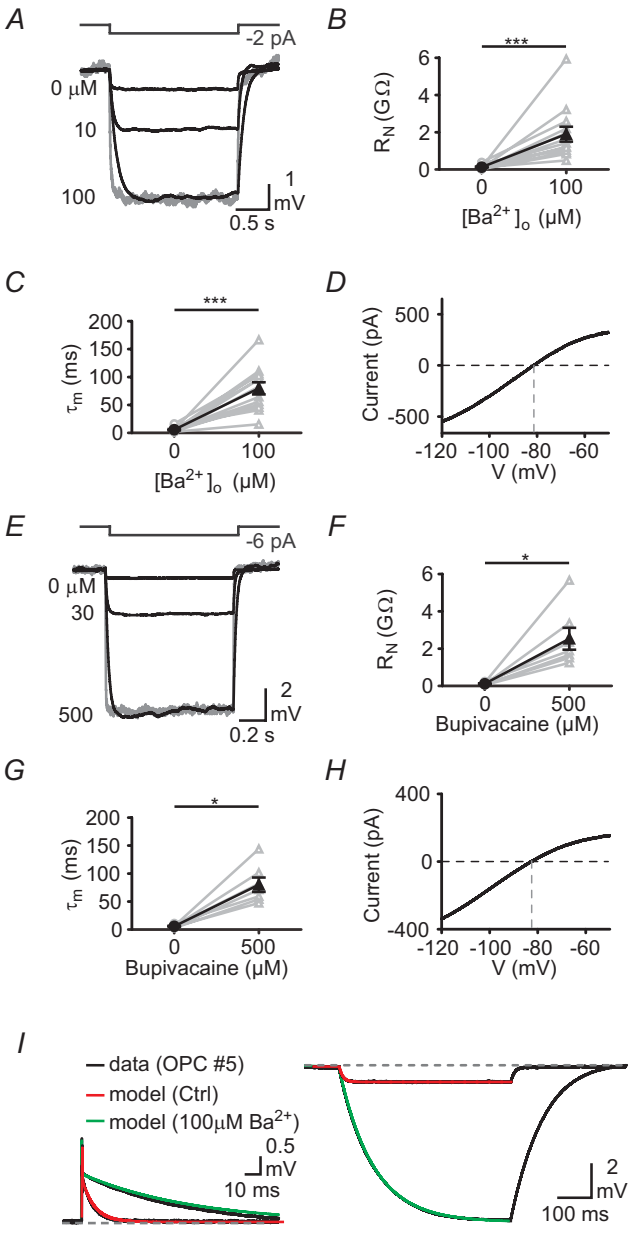

Figure 4. Ba^{2+} and bupivacaine-sensitive K^+ channels mediate resting conductance
A, voltage responses induced by a small hyperpolarizing pulse from the V_{rest} in control and in the presence of different Ba^{2+} concentrations. Trace in control was scaled (grey) to the peak of the response to Ba^{2+} (100 μM). *B*, summary of R_N in control and in the presence of Ba^{2+}; $^{***}P < 0.001$. Grey symbols connected by lines indicate data from the same experiment. *C*, summary of τ_m in control and in the presence of Ba^{2+}; $^{***}P < 0.001$. *D*, whole-cell recording of membrane current evoked by a voltage ramp (from −140 to −50 mV, 45 mV s^{-1}). The *I–V* relationship of Ba^{2+}-sensitive current obtained by digitally subtracting current in the presence of Ba^{2+} (100 μM) from that in control. *E*, voltage responses induced by a small hyperpolarizing pulse from the V_{rest} in control and after addition of bupivacaine. Trace in control was scaled (grey) for kinetics comparison. *F*, summary of R_N in control and in the presence of bupivacaine; $^{*}P < 0.05$. *G*, summary of τ_m in control and in the presence of bupivacaine; $^{*}P < 0.05$. *H*, bupivacaine-sensitive current obtained by digitally subtracting current in the presence of bupivacaine (500 μM) from that in control. *I*, short- and long-pulse data in control (Ctrl) and in the presence of 100 μM $BaCl_2$ and their fits.

Moreover, despite the difference in latency, all activated synapses along the processes resulted in little variation in decay of somatic EPSPs (Fig. 6*G*) as exemplified by the normalized somatic EPSP traces (Fig. 6*H*).

In contrast to powerful voltage attenuation from processes to soma, somatic voltage spread into processes was more efficient. This was evidenced by the spatial profile of transfer impedance (Z_c; Fig. 6*I*), which was computed by dividing the remote voltage change at the process by the current (100 Hz) signal injection at the soma (Fig. 6*J*). The steady-state voltage transfer ratio ($k_{soma \rightarrow syn}$), i.e. $V_{process}/V_{soma}$ was greater than 0.7 (Fig. 6*K*), indicating that OPCs are electrotonically compact. Together, the steady-state voltage control of processes from the soma is very good (Fig. 6*L*).

Comparison of simulated voltage attenuation with measured data

As OPCs have thin processes (Table 1), direct recordings on tiny processes with conventional patch pipettes are not possible. Therefore, we analysed OPC cable properties by performing simultaneous patch-electrode recordings from the soma and the relatively large proximal processes (mean diameter, 1.2 μm). First, OPCs were filled with a red fluorescent dye Alexa 594 (100 μM) during somatic recordings. After loading the dye, process recordings were made under a two-photon microscope (Fig. 7*A*). Voltage responses evoked by a long pulse via somatic injection led to little voltage attenuation at the process 14 μm from the soma (Fig. 7*B*). By contrast, marked voltage attenuation was observed at the soma when voltage responses were evoked at the process via process injection in the same OPC (Fig. 7*C*). The voltage transient at the process was substantially larger on process current injection because of the higher local Z_N. The comparison of the somatic transient evoked by dendritic injection (Fig. 7*C*, black trace) with the dendritic transient obtained with somatic injection (Fig. 7*C*, dashed red trace) shows that the propagated responses were virtually identical. The result of this reciprocity test (Fig. 7*D*) therefore indicates that propagation occurred in a linear system (Schmidt-Hieber *et al.* 2007).

As a test of how well our models simulated our experimental data, we plotted the experimental results obtained from simultaneous recordings from the soma and process of OPCs (4 cells with somatic injection; 3 cells with process injection) with simulated data

generated from models. As predicted by the simulation, the average $k_{soma \rightarrow syn}$ had relatively little change (Fig. 7*E*), whereas the average $k_{syn \rightarrow soma}$ declined from 1 at the soma to ∼0.4 at the process 20 μm from the soma (Fig. 7*F*). Overall, the simulation data are similar to the degree of measured voltage attenuation, indicating that our OPC models recapitulate the real OPC cable properties.

R_m determines temporal window of local EPSP summation

How do these cable properties affect the signalling characteristics of OPCs? To address this question, R_m and R_i were altered while the original OPC structure was maintained (Fig. 8*A*). First, we determined the effect of changes in R_m. Increasing R_m in all sections by a factor of 10 (to mimic the effect of Ba^{2+}; see Fig. 9) only slightly increased the local EPSP peak amplitude (Fig. 8*B*), from 15.7 mV (black) to 16.2 mV (red)) at the generated site. Notably, the decay of local and somatic EPSPs largely increased (red trace in Fig. 8*B*). The decay of local EPSP was fitted with a bi-exponential function with τ_{fast} of 1.5 ms (82%) and τ_{slow} of 127.3 ms (18%). The weighted time constant τ_w is 24.1 ms. Thus, the low value of R_m is a key factor that sharpens the EPSP and limits temporal summation of EPSPs. However, because distal EPSPs decayed much faster than the τ_m, temporal summation of local EPSPs at synaptic sites was thus still restricted to short time intervals. To determine the temporal window of EPSP summation at synaptic sites, we simulated two successive EPSPs with variable duration at the same site. The degree of temporal summation was quantified as an increment of EPSP (ΔEPSP) relative to the amplitude of a single EPSP alone and was plotted against the time interval (Fig. 8*A*). As a result, the integration window increased significantly when R_m was increased by a factor of 10 (Fig. 8*C*). Two successive EPSPs generated at the same site within 50 ms still resulted in substantial summation (Fig. 8*D*, red trace).

OPCs have a relatively smaller value of R_i compared with dentate granule cells (DGCs). We thus tested the effect of changes in R_i. Increasing R_i by a factor of ∼1.2, i.e. 200 Ω cm, a value comparable to that of DGCs, slightly increased the local EPSP peak amplitude (from 15.7 mV (black) to 17.2 mV (green)) without change of decay rate (Fig. 8*B* and *E*). With the original R_i, as determined by the fitting procedure, the time window of EPSP summation had a half-width of 3 ms. To estimate the contribution of the initial charge redistribution in shaping the time window, these simulations were repeated in the same model but with an increase of R_i to 200 Ω cm, yielding only a small increase in ΔEPSP (from 7.05 mV to 7.1 mV) and the time window (half-width from 3.0 ms to 3.4 ms). Nevertheless, an intermediate value of R_i is functionally essential for substantial EPSP summation because if R_i is set to be 0.1, the ΔEPSP during coincident synaptic events dramatically dropped (dashed line, Fig. 8*F*).

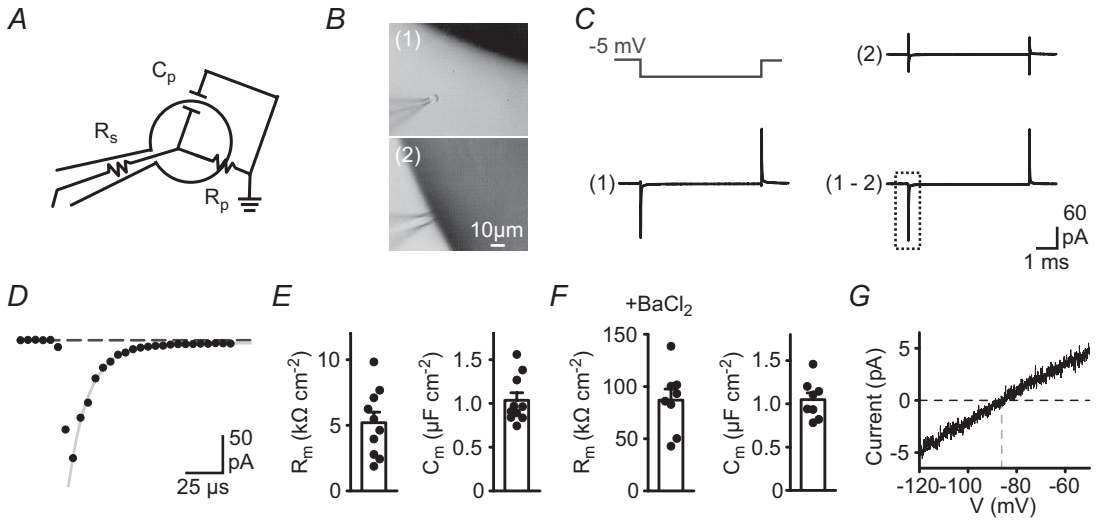

Figure 5. Direct measurements of R_m and C_m in OPCs
A, an equivalent circuit of the nucleated patch recording. *B*, a nucleated patch from an OPC was visualized using IR-DIC microscopy before (1) and after (2) being pressed against a small Sylgard ball. *C*, current transient (trace (1)) evoked by the voltage step from a nucleated patch. Trace (2), current transient after the patch pipette was pressed against a Sylgard ball with a GΩ seal; trace (1 – 2), current transient after subtraction. Expanded dotted square is shown in *D*. *D*, data points superimposed with an exponential fit. *E*, summary of R_m and C_m in control. *F*, summary of R_m and C_m in the presence of $BaCl_2$. *G*, Ba^{2+}-sensitive component was isolated in a nucleated patch recording using a voltage ramp (from −140 to 0 mV, 70 mV s^{-1}).

Background K^+ conductances attenuate EPSP amplitude and sharpen EPSP decay

To examine the functional relevance of low R_m in EPSP propagation and integration, we made whole-cell recordings from OPCs and focally applied hypertonic solution (500 mM sucrose in ACSF) across all cells to trigger vesicular release from nerve terminals (De Biase *et al.* 2010). In the presence of the antagonists for $GABA_A$ receptors (gabazine,1 μM) and Na_V channels (TTX, 0.5 μM), hypertonic solution elicited bursts of transient inward currents in OPCs (Fig. 9*A*) that were blocked by the AMPA receptor antagonist 6-cyano-7-nitroquinoxaline-2,3-dione (CNQX, 10 μM). The mEPSC amplitude (20.01 ± 1.33 pA, $n = 5$, Fig. 9*A*) and kinetics (mEPSC $\tau_{rise} = 0.26 \pm 0.03$ ms, $n = 5$; mEPSC $\tau_{decay} = 1.56 \pm 0.13$ ms, $n = 5$, Fig. 9*B*) were similar to those of simulated EPSCs detected from the soma (EPSC τ_{decay} range: from 1.2 to 1.8 ms; data not shown). In current clamp recordings, hypertonic solution elicited bursts of rapid mEPSPs (Fig. 9*C*) with the average peak amplitude of 0.80 ± 0.11 mV ($n = 8$; Fig. 9*E*) and τ_{decay} of 5.40 ± 0.93 ms ($n = 8$; Fig. 9*F*). In the presence of Ba^{2+} (100 μM), the duration of hypertonic solution-induced mEPSPs markedly increased (>10-fold; Fig. 9*D*, red trace), leading to significant summation of successive mEPSPs (Fig. 9*C*). On average, the peak amplitude and τ_{decay} of mEPSPs increased to 1.55 ± 0.18 mV ($n = 8$; $P < 0.01$, Wilcoxon signed-rank test, Fig. 9*E*) and 31.45 ± 5.07 ms ($n = 8$; $P < 0.01$,

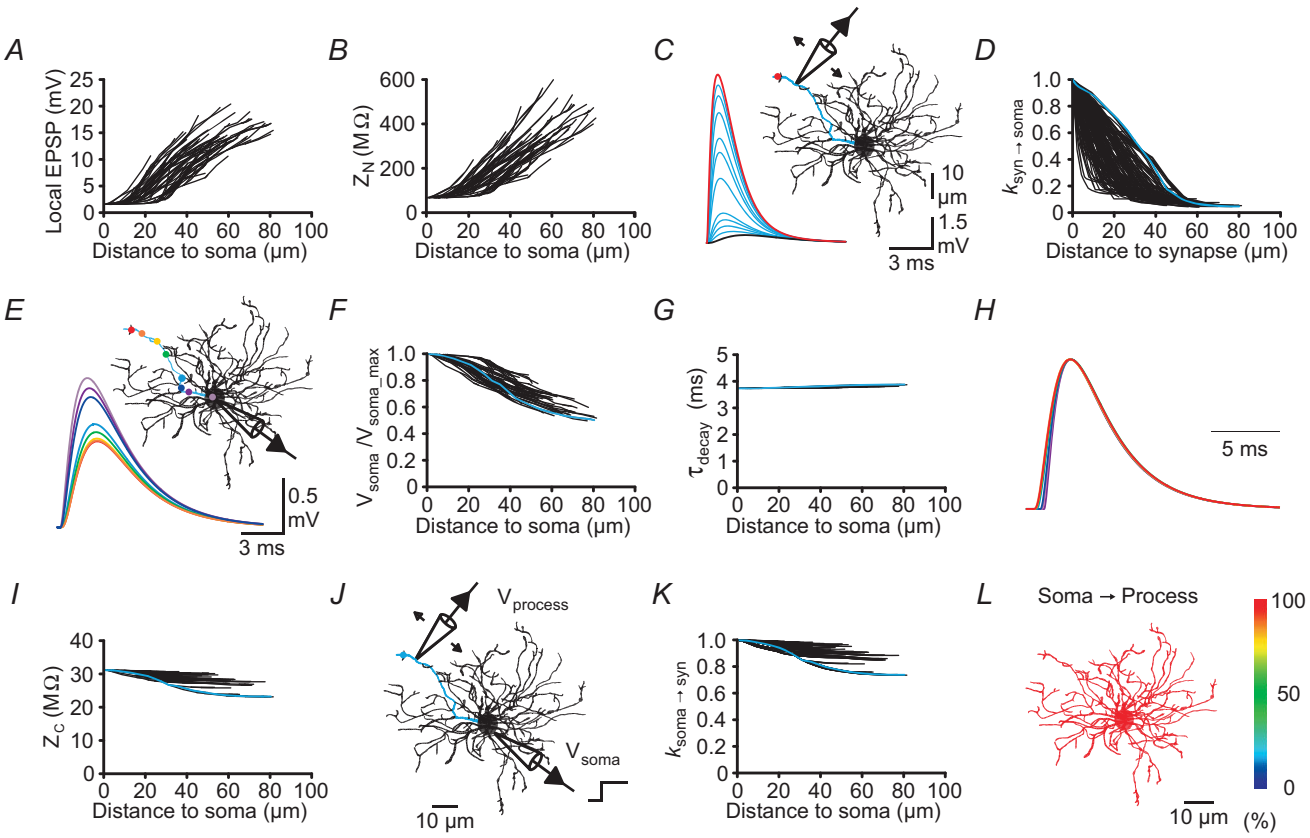

Figure 6. Rapid EPSP attenuation along OPC processes
A, local EPSP amplitude generated at a synapse plotted against the distance to soma. *B*, Z_N plotted against the distance to soma. *C*, an EPSP (red) generated at the synapse (red dot) attenuated along the blue path. Note that the time course of local EPSPs slowed along the path. *D*, voltage transfer ratio ($k_{syn \rightarrow soma}$) plotted against the distance to synapse. EPSPs were generated at the distal tips of processes. *E*, simulated synapses (colour-coded dots) placed along a process and a recording pipette at the soma. Example traces of somatic EPSPs generated at the colour-coded dots along the blue path. *F*, normalized somatic EPSP amplitude ($V_{soma}/V_{soma-max}$) plotted against the distance to soma. V_{soma} resulted from synapses placed at all locations along the process. $V_{soma-max}$ was the maximal V_{soma}. *G*, τ_{decay} of somatic EPSP. Note that the somatic EPSP time course was independent of synapse location. *H*, example traces of normalized somatic EPSPs. *I*, Z_c plotted against the distance to soma. *J*, diagram illustrating a DC voltage command applied by a pipette electrode at the soma and the local potential ($V_{process}$) measured at the process. *K*, voltage transfer ratio ($k_{soma \rightarrow syn}$) plotted against the distance to soma. *L*, colour-coded representation of steady-state voltage control of the processes by a voltage-clamp electrode located at the soma.

Wilcoxon signed-rank test, Fig. 9*F*), respectively, very similar to the modelling data (Fig. 8*B*, bottom trace, red)

We also examined the effect of Ba^{2+} on compound EPSPs evoked by electrical stimulation to Schaffer collaterals in the presence of antagonists for $GABA_A$Rs (gabazine, 1 μM), $GABA_B$Rs (CGP 55845, 1 μM) and NMDARs (D-AP5, 20 μM). Two compound EPSPs were evoked using a pair of pulses separated by an interval of 100 ms (Fig. 9*G*). On average, the peak amplitude and τ_{decay} of compound EPSP were 0.64 ± 0.19 mV ($n = 7$) and 3.85 ± 1.42 ms ($n = 7$), respectively (Fig. 9*H* and *I*). After addition of Ba^{2+}, the amplitude and decay of EPSPs were dramatically increased to 1.51 ± 0.31 mV ($n = 7$, $P < 0.05$, Wilcoxon signed-rank test) and 43.84 ± 12.51 ms ($n = 7$, $P < 0.05$, Wilcoxon signed-rank test), respectively (Fig. 9*H* and *I*). The summation of two successive EPSPs was also greatly enhanced (Fig. 9*G*). To summarize, large background K^+ conductances exert a powerful cable-filtering effect, which attenuates the EPSP amplitude and sharpens EPSP decay.

Discussion

This study represents the first investigation of cable properties underlying EPSP attenuation and integration in OPCs. By combining experiments and computational modelling, we show that a low value of R_m, which is largely mediated by Ba^{2+}- and bupivacaine-sensitive background K^+ channels, together with morphology are key determinants of EPSP attenuation and integration in OPCs.

Geometry and branching patterns contribute to synaptic normalization

Computational analysis of OPC models reveals that EPSP amplitude detected at the soma is much less dependent on synaptic location (Fig. 6*F*) as compared to CA1 and cortical layer 5 pyramidal neurons (Jaffe & Carnevale, 1999; Williams & Stuart, 2003). This normalizing effect on somatic EPSPs arises mainly from the specific morphological architecture of OPCs. The degree of passive normalization of EPSPs is a reflection of the spatial profile of Z_c (Jaffe & Carnevale, 1999; Fig. 6*I* in this study).

Along any branch of OPC processes, EPSPs generated at a distal process decline substantially toward the soma (Fig. 6*C*). According to the two-port theory, voltage transfer ratio from the synapse to the soma ($k_{syn \rightarrow soma}$) is Z_c/Z_N (also see eqn (7) in Jaffe & Carnevale, 1999). Since Z_N increases significantly with distance to the soma (Fig. 6*B*), the spatial profile of Z_c thus remains relatively independent of synapse location (Fig. 6*I*). What is the factor determining the spatial profile of Z_N in OPCs

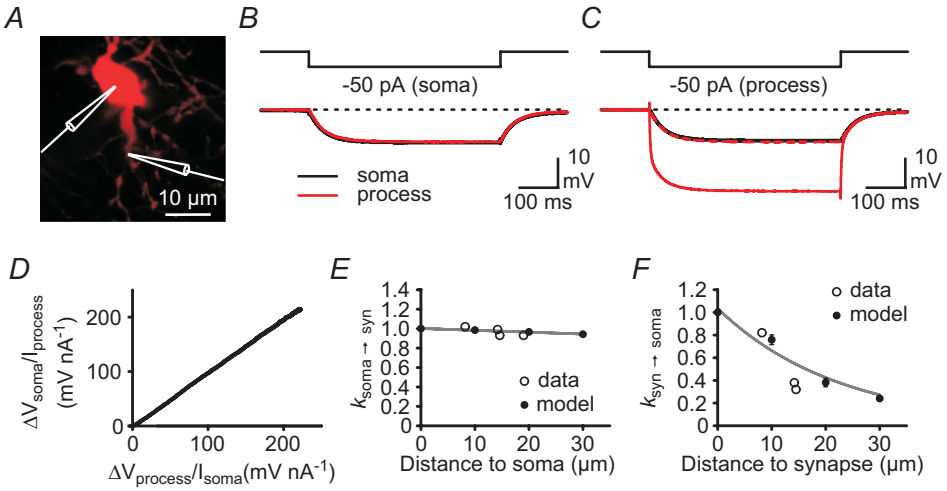

Figure 7. Test of reciprocity by dual recordings from the soma and the process
A, fluorescence image of an OPC filled with a red fluorescent dye Alexa 594 during simultaneous patch-electrode recordings from the soma and process. *B*, voltage responses evoked by somatic current injection. Black trace, somatic response; red trace, process response. *C*, voltage responses evoked by process current injection. Black trace, somatic response; red trace, process response; note that dashed red trace was the same process response as in *B*. *D*, test of reciprocity. Amplitudes of somatic voltage responses evoked by process current injection were plotted against process voltage responses evoked by somatic current injection at the same time point. Voltage responses were divided by the maximum of the injected current. *E*, comparison of steady-state somatic voltage attenuation of models with measured data. $k_{soma \rightarrow syn}$ is plotted for the average of all processes in a model cell OPC-1 at the indicated distance to the soma. Grey line corresponds to the model cell. The open circles are measured data. *F*, similar to *E*, $k_{syn \rightarrow soma}$ is plotted for the average of all processes in a model cell at the indicated distance to the synapses.

(Fig. 6*B*)? One possibility is the geometry resulting from the smaller diameter of distal processes coupled with their electrical isolation from the expanse of the soma (Williams & Stuart, 2003). The OPC processes taper very quickly once they emerge from the soma, which could lead to an increase of Z_N with distance from the soma (Fig. 6*B*) and account for passive normalization. However, dendritic branching pattern is also an important determinant (Jaffe & Carnevale, 1999). Hippocampal CA3 pyramidal neurons, CA3 interneurons and DGCs have the site-independence of Z_c (Jaffe & Carnevale, 1999; Schmidt-Hieber *et al.* 2007). These three types of neuron share a prominent morphological feature, that is, the lack of large and long primary dendrites. Therefore, it appears that the presence of a large primary dendrite is a prerequisite for significant location-dependent variability of Z_c (also see Jaffe & Carnevale, 1999). Together, the combination of process geometry and specific branching pattern may lead to the site independence of Z_c observed in OPCs.

Ionic basis of the low value of R_m in OPCs

OPCs have a strikingly low value of R_m as compared with those obtained from neurons under the same recording conditions (in the absence of $BaCl_2$ or CsCl). DGCs and cerebellar Purkinje cells have a high and homogeneous distribution of R_m. The mean R_m of DGCs is 38 kΩ cm^2 (Schmidt-Hieber *et al.* 2007). In the presence of the hyperpolarization-activated current (I_h) channel blocker ZD7288, cerebellar Purkinje cells have a mean R_m value of 122 kΩ cm^2 (Roth & Häusser, 2001). Even without blocked I_h conductance, the mean value of R_m in cerebellar Purkinje cells is about 20 kΩ cm^2. By contrast, the R_m of fast-spiking dentate basket cells is 7.6 kΩ cm^2 at proximal dendrites, 74.3 kΩ cm^2 at distal dendrites and 281 kΩ cm^2 at the axon (Nörenberg *et al.* 2010). Like DGCs and Purkinje cells, OPCs have uniform R_m. However, the R_m of OPCs is very low, suggesting high-density expression of background K^+ channels in OPCs. Indeed, Ba^{2+} and bupivacaine, both of which are known to block inwardly rectifying K^+ and tandem-pore

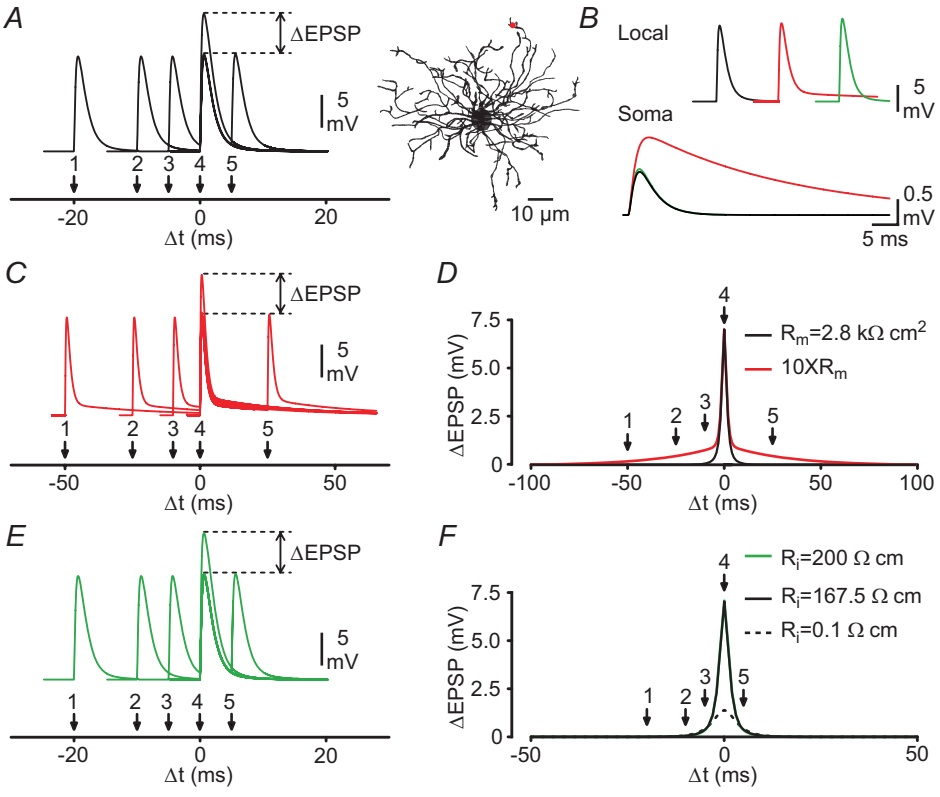

Figure 8. R_m defines the time window of EPSP summation
A, pairs of simulated EPSPs separated in time by 0–20 ms generated in a distal process (82 μm from the soma). Difference in EPSP (ΔEPSP) reflects the degree of temporal summation. Panel at right shows the reconstructed OPC-1 and the synaptic site (red dot) for simulations. *B*, top traces, local EPSPs at the same site as in *A* with default settings of the R_m and the R_i (black), a 10-fold R_m (red), and an increase in the R_i (green, 200 Ω cm); bottom traces, corresponding EPSPs at the soma. *C*, same as in *A* but with a 10-fold increase in the R_m. *D*, ΔEPSP plotted against the time interval (Δt) of the two simulated synaptic events. *E*, same as in *A*, but with the R_i set to 200 Ω cm. *F*, ΔEPSP plotted against the Δt of two simulated synaptic events.

TWIK-related acid-sensitive K^+ (TASK)-like channels, profoundly depolarized V_{rest} with a concomitant increase of R_m.

What is the possible molecular identity of background K^+ channels in OPCs? A recent study by Maldonado *et al*. (2013) has demonstrated that OPCs express a high abundance of Kir4.1 channels, a major conductance underlying a linear *I–V* relationship in OPCs. They also examined whether TASK-like channels were functionally expressed in OPCs because according to a transcriptome database, the mRNAs of the TASK-like channels TWIK1 and TREK1 are preferentially enriched in acutely isolated purified OPCs (Cahoy *et al*. 2008). However, the lack of effect of isoflurane in these currents (Maldonado *et al*. 2013) and the unchanged electrophysiological phenotype of OPCs in a transgenic mouse expressing inactivated TWIK1 show that, contrary to astrocytes, TASK-like channels are poorly expressed in OPCs. In conclusion, Kir4.1 channels appear to be the major component of background K^+ channels in OPCs, although we cannot exclude the presence of additional channels with small contributions.

Comparison of R_m with other glial cells

Within the oligodendrocyte lineage, the passive electrical properties of oligodendroglial cells are developmentally modified. $NG2^+$ OPCs have a modest value of R_m (on average, 4.1 kΩ cm^2 estimated by cable fitting and 5.2 kΩ cm^2 by direct measurement in this study; 5.8 kΩ cm^2 in De Biase *et al*. 2010; but note 13 kΩ cm^2

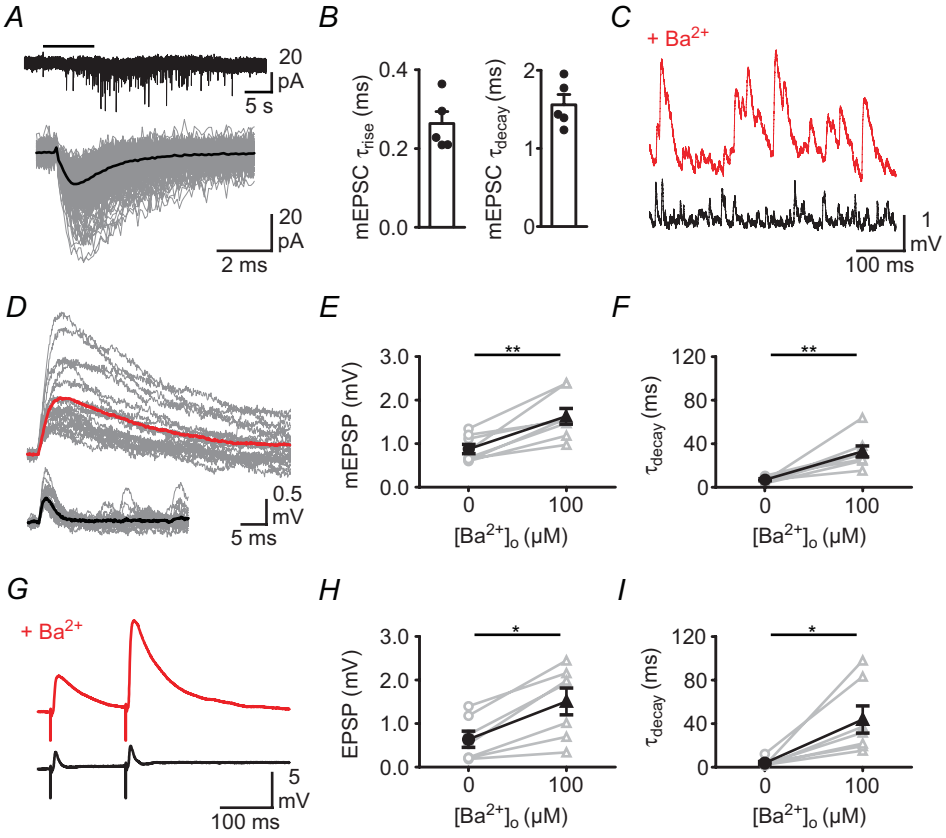

Figure 9. Ba^{2+} increased EPSP amplitude and prolonged EPSP decay
A, top, hypertonic solution (500 mM sucrose in ACSF) induced vesicular glutamate release at neuron–OPC synapses. Bottom, superimposed mEPSC traces (grey) and an average mEPSC trace (black, average of 356 events). Horizontal bar indicates time of application of sucrose solution. *B*, summary of average mEPSC τ_{rise} and τ_{decay}. *C*, similar to *A*, mEPSPs recorded in control (black) and in the presence of Ba^{2+} (red). Note significant EPSP summation in the presence of Ba^{2+}. *D*, superimposed single mEPSP traces (grey; bottom, control; top, in the presence of Ba^{2+}) and average mEPSP traces (black, control, average of 34 events; red, Ba^{2+}, average of 24 events). *E*, summary of mEPSP amplitude before and after addition of Ba^{2+}; $^{**}P < 0.01$. *F*, summary of mEPSP τ_{decay} before and after addition of Ba^{2+}; $^{**}P < 0.01$. *G*, electrically evoked compound EPSPs before and after addition of Ba^{2+} (100 μM). Note the temporal summation of EPSPs in the presence of Ba^{2+}. Each trace is average of 10 sweeps. *H*, summary of EPSP amplitude before and after addition of Ba^{2+}; $^{*}P < 0.05$. *I*, summary of EPSP τ_{decay} before and after addition of Ba^{2+}; $^{*}P < 0.05$.

reported by Kukley *et al*. 2010) as compared with those of Pre-OLs (~32.5 kΩ cm^2 in De Biase *et al*. 2010; ~133.8 kΩ cm^2; Kukley *et al*. 2010) and OLs (~2.8 kΩ cm^2 in De Biase *et al*. 2010; ~5.2 kΩ cm^2 in Kukley *et al*. 2010).

Significant differences in passive membrane properties between OPCs and microglia but not astrocytes were noted. Microglia have a similar membrane capacitance (~30 pF) to OPCs, but relatively higher membrane resistance (>1 GΩ); the estimated value of R_m is about 40 kΩ cm^2 (Wu & Zhou, 2008). Unlike other types of glial cells, astrocytes form extensive gap junctions. Therefore, astrocyte recordings in brain slices may introduce shunt artifacts (Chu *et al*. 2010). In acutely isolated astrocytes, the estimated value of R_m depends on the postnatal age and varies by almost an order of magnitude (0.88–8.4 kΩ cm^2; Matthias *et al*. 2003).

Functional relevance of the low R_m

Activation of Ca_v channels provokes Ca^{2+} elevations in OPCs (Haberlandt *et al*. 2011). However, tetanic stimulation of presynaptic neurons causes postsynaptic currents but no somatic $[Ca^{2+}]_i$ elevations, suggesting that $[Ca^{2+}]_i$ elevations in OPCs might be restricted to their processes (Haberlandt *et al*. 2011). This is consistent with powerful EPSP attenuation along OPC processes. Furthermore, with a low R_m, local EPSP summation requires high temporal precision. Our simulation data show that the summation of two successive EPSPs at generated sites must occur within the 10 ms time window, which appears to be unlikely to occur in OPCs in brain slices (<0.01 Hz in Bergles *et al*. 2000; De Biase *et al*. 2010; 0.006 Hz, $n = 6$, our observation). However, if OPCs *in vivo* could receive high-frequency (>100 Hz) or synchronous synaptic inputs, summation of rapid EPSPs could occur. What could be the possible physiological function? Like neuronal growth cones, we speculate that coincident detection of EPSPs will result in local Ca^{2+} elevation in OPC processes, thus affecting the mobility of OPC processes (Haberlandt *et al*. 2011; Hughes *et al*. 2013). The future work is to determine the physiological rates of EPSPs in OPCs *in vivo*.

In the model, an increase in R_m significantly increases the somatic EPSP amplitude and prolongs the somatic EPSP half-duration (Fig. 8*B*). Experimentally, an increase in R_m by Ba^{2+} significantly attenuates the cable-filtering effect, thus increasing the somatic EPSP amplitude, duration and temporal summation (Fig. 9*C* and *G*). Notably, because the time course of synaptic conductance mediated by AMPA receptors is extremely rapid, the amplitudes of EPSPs at generated sites are, therefore, largely independent of membrane resistance (Fig. 8*B*; also see Williams & Stuart, 2003).

In addition to the synaptic integration, the leaky membrane property of OPCs may have potential relevance to pathological changes that occur following ischaemia. Prolonged exposure to glutamate causes excitotoxic degeneration (McDonald *et al*. 1998). Although glutamate-mediated transmission is important for OPC proliferation, migration and differentiation (Gallo *et al*. 1996; Yuan *et al*. 1998; Gudz *et al*. 2006; Mangin & Gallo, 2011), they also render OPCs susceptible to ischaemic damage in early development (Pellegrini-Giampietro *et al*. 1997). Excessive excitation to OPCs can lead to the opening of Ca_v channels (Haberlandt *et al*. 2011) and result in Ca^{2+}-dependent excitotoxicity. Thus, large background K^+ conductances of OPCs may limit the extent of membrane depolarization under pathophysiological conditions.

References

Bergles DE, Roberts JD, Somogyi P & Jahr CE (2000). Glutamatergic synapses on oligodendrocyte precursor cells in the hippocampus. *Nature* **405**, 187–191.

Cahoy JD, Emery B, Kaushal A, Foo LC, Zamanian JL, Christopherson KS, Xing Y, Lubischer JL, Krieg PA, Krupenko SA, Thompson WJ & Barres BA (2008). A transcriptome database for astrocytes, neurons, and oligodendrocytes: a new resource for understanding brain development and function. *J Neurosci* **28**, 264–278.

Carnevale NT & Hines ML (2006). *The Neuron Book*. Cambridge University Press, Cambridge, UK.

Carnevale NT & Johnston D (1982). Electrophysiological characterization of remote chemical synapses. *J Neurophysiol* **47**, 606–621.

Chittajallu R, Aguirre A & Gallo V (2004). NG2-positive cells in the mouse white and grey matter display distinct physiological properties. *J Physiol* **561**, 109–122.

Chu KC, Chiu CD, Hsu TT, Hsieh YM, Huang YY & Lien CC (2010). Functional identification of an outwardly rectifying pH- and anaesthetic-sensitive leak K^+ conductance in hippocampal astrocytes. *Eur J Neurosci* **32**, 725–735.

De Biase LM, Nishiyama A & Bergles DE (2010). Excitability and synaptic communication within the oligodendrocyte lineage. *J Neurosci* **30**, 3600–3611.

Drummond GB (2009). Reporting ethical matters in *The Journal of Physiology*: standards and advice. *J Physiol* **587**, 713–719.

Gallo V, Mangin JM, Kukley M & Dietrich D (2008). Synapses on NG2-expressing progenitors in the brain: multiple functions? *J Physiol* **586**, 3767–3781.

Gallo V, Zhou JM, McBain CJ, Wright P, Knutson PL & Armstrong RC (1996). Oligodendrocyte progenitor cell proliferation and lineage progression are regulated by glutamate receptor-mediated K^+ channel block. *J Neurosci* **16**, 2659–2670.

Ge WP, Yang XJ, Zhang Z, Wang HK, Shen W, Deng QD & Duan S (2006). Long-term potentiation of neuron-glia synapses mediated by Ca^{2+}-permeable AMPA receptors. *Science* **312**, 1533–1537.

Gentet LJ, Stuart GJ & Clements JD (2000). Direct measurement of specific membrane capacitance in neurons. *Biophys J* **79**, 314–320.

Gudz TI, Komuro H & Macklin WB (2006). Glutamate stimulates oligodendrocyte progenitor migration mediated via an α_v integrin/myelin proteolipid protein complex. *J Neurosci* **26**, 2458–2466.

Haberlandt C, Derouiche A, Wyczynski A, Haseleu J, Pohle J, Karram K, Trotter J, Seifert G, Frotscher M, Steinhäuser C & Jabs R (2011). Gray matter NG2 cells display multiple Ca^{2+}-signaling pathways and highly motile processes. *PLoS One* **6**, e17575.

Hines ML & Carnevale NT (1997). The NEURON simulation environment. *Neural Comput* **9**, 1179–1209.

Hughes EG, Kang SH, Fukaya M & Bergles D (2013). Oligodendrocyte progenitors balance growth with self-repulsion to achieve homeostasis in the adult brain. *Nat Neurosci* **16**, 668–676.

Jaffe DB & Carnevale NT (1999). Passive normalization of synaptic integration influenced by dendritic architecture. *J Neurophysiol* **82**, 3268–3285.

Kukley M, Nishiyama A & Dietrich D (2010). The fate of synaptic input to NG2 glial cells: neurons specifically downregulate transmitter release onto differentiating oligodendroglial cells. *J Neurosci* **30**, 8320–8331.

Lin YC, Liu YC, Huang YY & Lien CC (2010). High-density expression of Ca^{2+}-permeable ASIC1a channels in NG2 glia of rat hippocampus. *PLoS One* **5**, e12665.

McDonald JW, Levine JM & Qu Y (1998). Multiple classes of the oligodendrocyte lineage are highly vulnerable to excitotoxicity. *Neuroreport* **9**, 2757–2762.

Maldonado PP, Vélez-Fort M, Levavasseur F & Angulo MC (2013). Oligodendrocyte precursor cells are accurate sensors of local K^+ in mature grey matter. *J Neurosci* **33**, 2432–2442.

Mangin JM & Gallo V (2011). The curious case of NG2 cells: transient trend or game changer? *ASN Neuro* **3**, e00052.

Matthias K, Kirchhoff F, Seifert G, Hüttmann K, Matyash M, Kettenmann H & Steinhäuser C (2003). Segregated expression of AMPA-type glutamate receptors and glutamate transporters defines distinct astrocyte populations in the mouse hippocampus. *J Neurosci* **23**, 1750–1758.

Myatt DR, Hadlington T, Ascoli GA & Nasuto SJ (2012). Neuromantic – from semi-manual to semi-automatic reconstruction of neuron morphology. *Front Neuroinform* **6**, 4.

Nishiyama A, Komitova M, Suzuki R & Zhu X (2009). Polydendrocytes (NG2 cells): multifunctional cells with lineage plasticity. *Nat Rev Neurosci* **10**, 9–22.

Nörenberg A, Hu H, Vida I, Bartos M & Jonas P (2010). Distinct nonuniform cable properties optimize rapid and efficient activation of fast-spiking GABAergic interneurons. *Proc Natl Acad Sci U S A* **107**, 894–899.

Pellegrini-Giampietro DE, Gorter JA, Bennett MV & Zukin RS (1997). The GluR2 (GluR-B) hypothesis: Ca^{2+}-permeable AMPA receptors in neurological disorders. *Trends Neurosci* **20**, 464–470.

Rall W (1964). Theoretical significance of dendritic trees for neuronal input–output relations. In *Neural Theory and Modeling*, ed. R. F. Reiss, pp. 73–97. Stanford University Press, Palo Alto, CA, USA.

Roth A & Häusser M (2001). Compartmental models of rat cerebellar Purkinje cells based on simultaneous somatic and dendritic patch-clamp recordings. *J Physiol* **535**, 445–472.

Schmidt-Hieber C, Jonas P & Bischofberger J (2007). Subthreshold dendritic signal processing and coincidence detection in dentate gyrus granule cells. *J Neurosci* **27**, 8430–8441.

Taverna S, Tkatch T, Metz AE & Martina M (2005). Differential expression of TASK channels between horizontal interneurons and pyramidal cells of rat hippocampus. *J Neurosci* **25**, 9162–9170.

Williams SR & Stuart GJ (2003). Role of dendritic synapse location in the control of action potential output. *Trends Neurosci* **26**, 147–154.

Wu LJ & Zhuo M (2008). Resting microglial motility is independent of synaptic plasticity. *J Neurophysiol* **99**, 2026–2032.

Yuan X, Eisen AM, McBain CJ & Gallo V (1998). A role for glutamate and its receptors in the regulation of oligodendrocyte development in cerebellar tissue slices. *Development* **125**, 2901–2914.

Zhou W, Arrabit C, Choe S & Slesinger PA (2001). Mechanism underlying bupivacaine inhibition of G protein-gated inwardly rectifying K^+ channels. *Proc Natl Acad Sci U S A* **98**, 6482–6487.

Additional information

Competing interests

None declared.

Author contributions

C.-F.C., J.-Y.W. and T.-Y.C.: whole-cell recordings, experimental design, data analysis and interpretation; T.-W.K.: cable modelling, simulations and data interpretation; Y.-C.L.: dual soma and process recordings, data analysis and interpretation; J.-K.C.: experimental design and data interpretation; C.-C.L.: project conception, experimental design, data analysis and interpretation, and drafting the manuscript. All authors approved the final version of the manuscript. All experiments were carried out at the National Yang-Ming University, Taipei, Taiwan.

Funding

This work was supported by grants from the Ministry of Education, Aim for the Top University Plan, National Health Research Institutes (NHRI-EX100-9720NC), National Science Council (NSC101-2321-B-010-024 and NSC99-2321-B-010-001 to C.-C.L.; NSC98-2314-B-195-002-MY3 to J.-K.C.) and Cheng Hsin General Hospital (grant nos 100-53 and 100F117CY19).

Acknowledgements

We thank M. M. Poo, D. Engel, P. Geshwill and M. Martina for helpful advice and critical reading of the manuscript.